International Journal of Steel Structures 15(4): 785-795 (2015)
DOI 10.1007/s13296-015-1202-x
ISSN 1598-2351 (Print)
ISSN 2093-6311 (Online)

International Journal of
STEEL
STRUCTURES
www.springer.com/journal/13296

Lateral Compression Behaviors of Thin-walled Equilateral Triangular Tubes

Hualin Fan[1,2,*], Wu Hong[2], Fangfang Sun[2,3,*], Ying Xu[2,*], and Fengnian Jin[2,*]

[1]*State Key Laboratory of Mechanics and Control of Mechanical Structures, Nanjing University of Aeronautics and Astronautics, Nanjing, 210016, China*
[2]*State Key Laboratory for Disaster Prevention & Mitigation of Explosion & Impact, PLA University of Science & Technology, Nanjing, 210007, China*
[3]*Laboratory of Structural Analysis for Defense Engineering and Equipment, College of Mechanics and Materials, Hohai University, Nanjing, 210098, China*
[4]*State Key Laboratory of Structural Analysis for Industrial Equipment, Dalian University of Technology, Dalian, 116023, China*

Abstract

The paper deals with one important topic in impact engineering - the lateral compression behavior of thin-walled tubes. To study the lateral collapse modes and energy absorption behaviors of equilateral triangular tubes, quasi-static compression experiments were carried out. Crushing modes were revealed by the experiments. Three typical crushing stages characterize the lateral deformation plateaus of equilateral triangular tubes. In simulation, perfect tubes have symmetrical crushing modes. Strengths of the tubes were correctly predicted by the competition between yielding and buckling. Based on the observed crushing modes, plastic models were proposed for each stage to predict the lateral crushing behaviors theoretically. Equilateral triangular tubes have unified energy absorbing mechanisms, including five plastic hinges and one traveling plastic hinge. Plastic models have been constructed to predict the mean crushing forces and evaluate the energy absorption efficiency of the equilateral triangular tubes.

Keywords: equilateral triangular tube, lateral compression, crushing mechanism, plastic analysis

1. Introduction

Crushing behaviors of thin-walled tubular structures have received extensive attentions (Zhang and Zhang, 2012) for the potential application in energy absorber devices as the core layer of sandwich panels. Jones (1989) investigated two generic types of plastically deforming structures in energy absorbing situations which usually be applied as energy absorber devices. The both were similar to column structures collapse under axial compression. Radford *et al*. (2009) and Ferri *et al*. (2007) studied the dynamic response of square-honeycomb core, the I-core and the pyramidal truss core through direct impact experiments and finite element calculations. These studies discovered that micro-inertial stabilization significantly delayed the onset of buckling in these lattice cores. Lee *et al*. (2008) also carried out similar research works and surveyed the forces on both the impacted and distal faces of the sandwich cores. Crushing behavior of collapsible energy absorber devices with circular and elliptical cross-section subjected to different loading conditions had been investigated both experimentally and numerically (Mahdi and Hamouda; 2012). Hou *et al*. (2008; 2011) suggested multi-objective optimization of thin-walled tubes for the crashworthiness design based on their axial crushing behaviors.

Triangular tubes can be used as core layer of sandwich panels. Hong *et al*. (2013; 2014) and Fan *et al*. (2013) revealed the plastic deformation and energy absorption of triangular tubes under axial compression through experiments and theoretical analysis. However, performances of triangular tubes under lateral compression are rarely reported. Rejab and Cantwell (2013) revealed the triangular corrugated-core would take on a trapezium shape in crushing. Gupta *et al*. (2001) presented experimental and computational investigation of the deformation and energy absorbing

Received August 28, 2014; accepted April 1, 2015;
published online December 31, 2015

*Corresponding authors
E-mail:
fhl02@mails.tsinghua.edu.cn (Hualin Fan)
sunff1986@126.com (Fangfang Sun)
xuying72@163.com(Ying Xu)
jinfn2009@163.com (Fengnian Jin)

behaviour of rectangular and square tubes of aluminum and mild steel under lateral compression. It is seen that the tube section collapses on account of formation of two sets of plastic hinges. Abdewi *et al*. (2008) studied the lateral crushing behaviors of radial corrugated composite tubes. Dynamic buckling of an inclined strut was reported by McShane *et al*. (2012). Actually, it is a triangular thin-walled tubular core. They proposed a three-hinge plastic buckling mode of wavelength equal to the strut length in quasi-static compression. Wang *et al*. (2015) discussed crushing behaviors of thin-walled isosceles triangular tubes (ITTs). Tran *et al*. (2014) discussed crushing and crashworthiness of multi-cell triangular tubes through theoretical analyses and crashworthiness optimization.

Although similar approach has been explored for lateral crushing of prismatic tubes, lateral crushing behaviors of triangular tubes are rare. This paper adopted experiments, numerical simulations and theoretical analyses to investigate plastic deformation modes and energy absorption characteristics of laterally crushed equilateral triangular tubes (ETTs).

2. Experiments

Lateral crushing behaviors of ETTs were firstly studied, as shown in Fig. 1. All specimens were fabricated by mild steel Q235, whose mechanical constants were suggested by standard tensile experiments. Each ETT has a fixed length, b =50 mm, and wall thickness, t =3.0 mm. Breadth, L, varies from 30, 90, 120 to 150 mm. Only tube S1 has a tube length of 100 mm. Corresponding information is listed in Table 1.

Lateral compression experiments were carried out at a loading rate of 2.5 mm/min. As shown Fig. 2, typical deformation curves of ETTs with different breadth are of geometrical similarity. After the elastic deformation and the initial peak load, elastic or plastic buckling leads the load drop abruptly. Then rotations of plastic hinges maintain the deformation plateau. In lateral compression, ETTs have three typical plastic deformation plateaus, named as stage A, stage B and stage C. The third stage is divided into two sub-stages, stage C_1 and stage C_2. Each stage has a stable deformation plateau. Stress level of each plateau gradually increases, letting ETTs have excellent energy absorption in lateral compression.

Progressive lateral crushing modes of S1, S2 and S4 are figured in Fig. 3. Deformation modes of S3 are further simplified and modeled in Fig. 4 to promote the theoretical analysis. All ETTs have similar boot-like deformation modes.

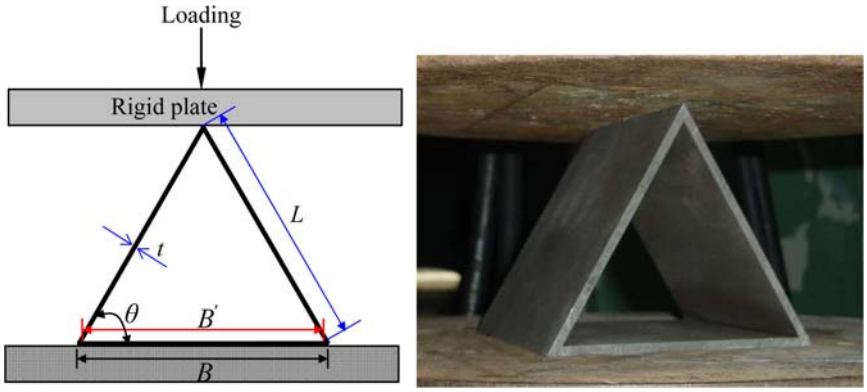

Figure 1. Specimen of ETT under lateral compression.

Table 1. Tested and predicted MCFs of ETTs

Specimen	Length (mm)	Breadth (mm)	Base angle	Tested data (kN)				Prediction (kN)			
				P_{max}	P_{mA}	P_{mB}	P_{mC}	P_{mA}	P_{mB}	P_{mC}	P_{max}
S1-1				103.7	47.49	72.03	127.38				
S1-2	100	30	60^0	108.2	48.54	71.66	125.15	41.84	73.40	132.50	122.1
S1-3				110.4	48.68	83.49	136.60				
S2-1				55.04	9.35	15.99	30.74				
S2-2	50	90	60^0	50.43	8.72	14.99	28.56	6.97	12.23	22.08	61.05 (Yielding); 58.77 (Buckling)
S2-3				44.78	8.70	15.0	28.56				
S3-1	50	150	60^0	28.47	3.93	8.35	16.90	4.18	7.34	13.25	21.16
S4-1				13.75	3.97	6.75	12.46				
S4-2	50	180	60^0	13.37	3.97	6.42	12.57	3.49	6.12	11.04	14.69
S4-3				13.32	3.97	6.75	12.70				

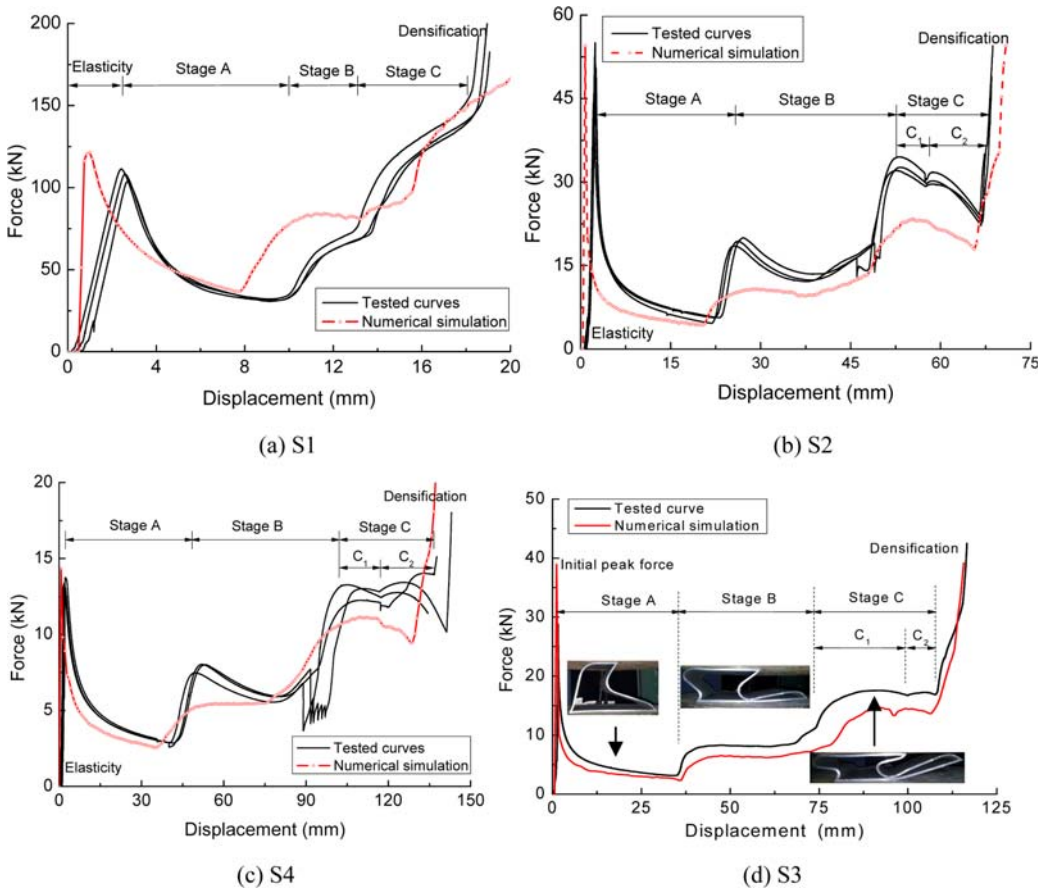

Figure 2. Lateral compression curves of ETTs.

3. Analyses

3.1. Strength

Tubes S1 and S2 have close initial peak loads, while peak loads of S3 and S4 decrease greatly. Controlled by steel yielding, the initial peak load, $P_{\max}$, is predicted by

$$P_{\max}=\sqrt{3}\sigma_y tb\,, \tag{1}$$

where yielding strength σ_y=235 MPa. The predicted load is 61.05 kN. With slender walls, the initial peak load of the tube will be controlled by elastic buckling as

$$P_{\max}=\frac{\sqrt{3}\pi^2 Ebt^3}{12(\mu L)^2}\,. \tag{2}$$

With constraint coefficient μ=0.7 and Young's modulus E=210 GPa, $P_{\max}$=0.824/L^2 kN. A critical breadth, L_c, is suggested by Eqs. (1) and (2) as

$$L_c=\frac{\pi t}{\mu}\sqrt{\frac{E}{12\sigma_y}} \tag{3}$$

to decide the transition from yielding to buckling. Here, L_c=0.116 m. Accordingly, strengths were predicted, as shown in Fig. 5, where b=50 mm. Strength of S1 with b=50 mm is 61.05 kN predicted by Eq. (1), very close to a half of the tested value for S1 with b=100 mm. Tube S2 has close dimension to the critical breadth, so tested strength of S2 is consistent with the prediction of Eq. (1), as well as Eq. (2). Tested strengths of S3 and S4 are close to predictions of Eq. (2).

3.2. Stage A

As shown in Fig. 4, in stage A the two inclined sides fell into buckling simultaneously. One bended outwardly and the other inwardly. As a result, plastic hinges D and E formed and divided each side into two parts. The upper segments, AD and AE, rotated around the corner. The lower segments, DB and EC have smaller rotations, forming other two plastic hinges, B and C. The angle of corner A kept invariable in rotation. The length ratios of the upper segment length to the whole length were nearly the same as one third. Corner A did not move horizontally. Segment AD was completely crushed to adhere to the loading cell at the end of stage A. Detailed information, including strength and mean crushing force, was listed in Table 1.

Typical folding mechanism was simplified in Fig. 6. Lengths of AD, BD, AE and EC are λL, $(1-\lambda)L$, ηL, and

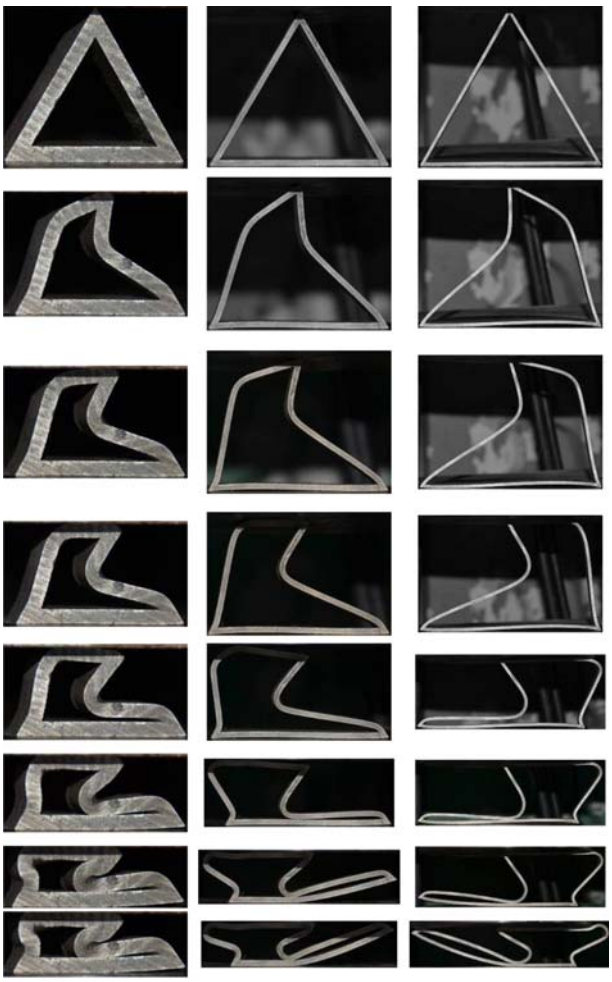

Figure 3. Lateral progressive crushing of ETTs.

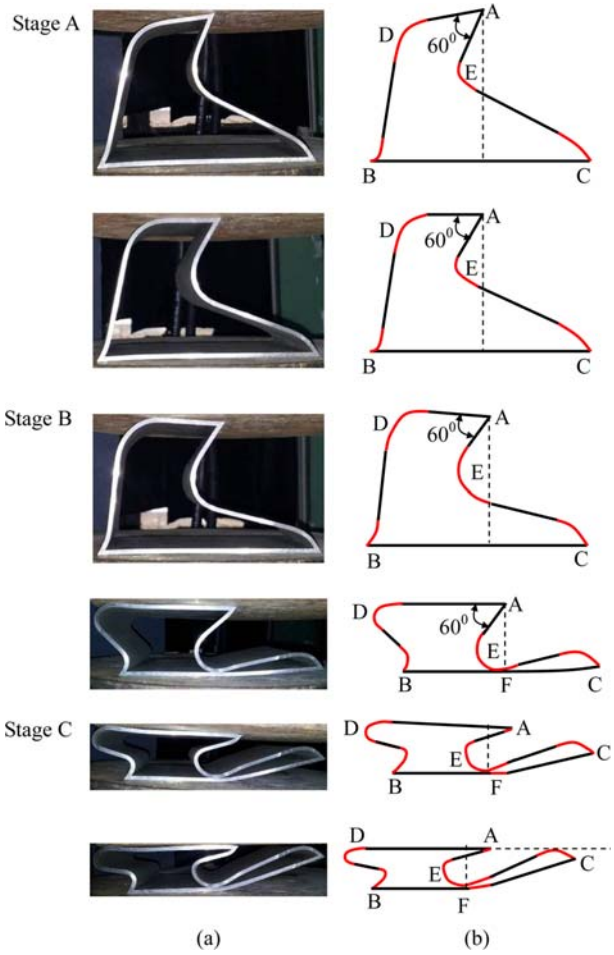

Figure 4. Typical (a) deformation modes and (b) corresponding plastic models of S3.

$(1-\eta)L$, respectively. The angle between DB and BA' is defined by α. Similarly, the angle between EC and CA' is β. Rotation angles of plastic hinges D, B, E and C are $\alpha+\pi/3$, α, $\beta+\pi/3$, and β, respectively. Crushing displacement in stage A, Δ_1, is

$$\Delta_1=AA'=\sqrt{3}\,AD'=\sqrt{3}\,\lambda L-2(1-\lambda)L\sin\alpha \tag{4}$$

from AD',

$$\Delta_1 = A'B\sin\left(\frac{\pi}{3}\right)-DB\sin\left(\frac{\pi}{3}+\alpha\right)=\frac{\sqrt{3}}{2}L\left[1-(1-\lambda)\cos\alpha-\frac{\sqrt{3}}{3}(1-\lambda)\sin\alpha\right] \tag{5}$$

from DB and

$$\Delta_1 = (A'C-AE)\sin\left(\frac{\pi}{3}\right)-EC\sin\left(\frac{\pi}{3}-\beta\right)=\frac{\sqrt{3}}{2}(1-\eta)L-(1-\eta)L\sin\left(\frac{\pi}{3}-\beta\right) \tag{6}$$

from AE and EC, respectively. Above equations suggest relations among variables as

$$\begin{cases}\sqrt{3}\lambda L-2(1-\lambda)L\sin\alpha=\dfrac{\sqrt{3}}{2}L-\dfrac{\sqrt{3}}{2}\eta L-(1-\eta)L\sin\left(\dfrac{\pi}{3}-\beta\right)\\ \dfrac{\sqrt{3}}{2}L\left[1-(1-\lambda)\cos\alpha-\dfrac{\sqrt{3}}{3}(1-\lambda)\sin\alpha\right]=\dfrac{\sqrt{3}}{2}L-\dfrac{\sqrt{3}}{2}\eta L-(1-\eta)L\sin\left(\dfrac{\pi}{3}-\beta\right)\end{cases}. \tag{7}$$

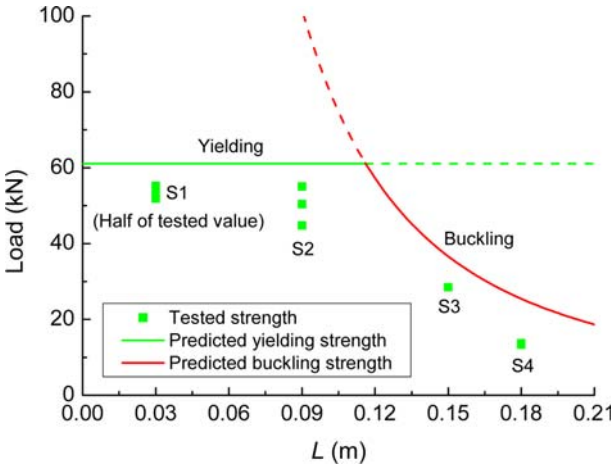

Figure 5. Predictions of initial peak loads.

Let

$$\kappa = \sqrt{3}\,\eta L + 2(1-\eta)L\sin\left(\frac{\pi}{3}-\beta\right), \tag{8}$$

then we get

$$\begin{cases} \lambda = \dfrac{3L^2-\kappa^2}{4(L^2+\kappa^2)} \\ \alpha = \arctan\left(\dfrac{\sqrt{3}L^2-\sqrt{3}\kappa^2+2L\kappa}{L^2+\kappa^2}\right) \end{cases}. \tag{9}$$

In the crushing, work done by the mean crushing force (MCF), P_{mA}, is equal to the plastic energy dissipated by the plastic hinges with rotations, φ_i, as

$$\sum_i^n M_p\varphi_i = P_{mA}\Delta_1 \tag{10}$$

with

$$M_p = \frac{1}{4}\sigma_p t^2 L, \tag{11}$$

where M_p is the full plastic moment of the solid wall and $\sigma_p=(\sigma_y+\sigma_u)/2$ is plastic stress of the steel, 316 MPa adopted here with ultimate collapse strength σ_u=397 MPa. The value of M_p is 35.55 N·m. Equation (10) is extended to be

$$M_p\left[\alpha+\beta+\left(\alpha+\frac{\pi}{3}\right)+\left(\frac{\pi}{3}+\beta\right)\right] = P_{mA}[\sqrt{3}\lambda L-2(1-\lambda)L\sin\alpha] \tag{12}$$

$$\frac{P_{mA}}{M_p} = \frac{8\left[\arctan\left(\dfrac{\sqrt{3}L^2-\sqrt{3}\tilde{\eta}^2+2L\tilde{\eta}}{\tilde{\eta}^2+L^2}\right)+\beta+\dfrac{\pi}{3}\right][L^2+\tilde{\eta}^2]}{(3L^2-\tilde{\eta}^2)\sqrt{3}L-8(L^2+\tilde{\eta}^2)L\sin\alpha+2(3L^2-\tilde{\eta}^2)L\sin\alpha} \tag{14}$$

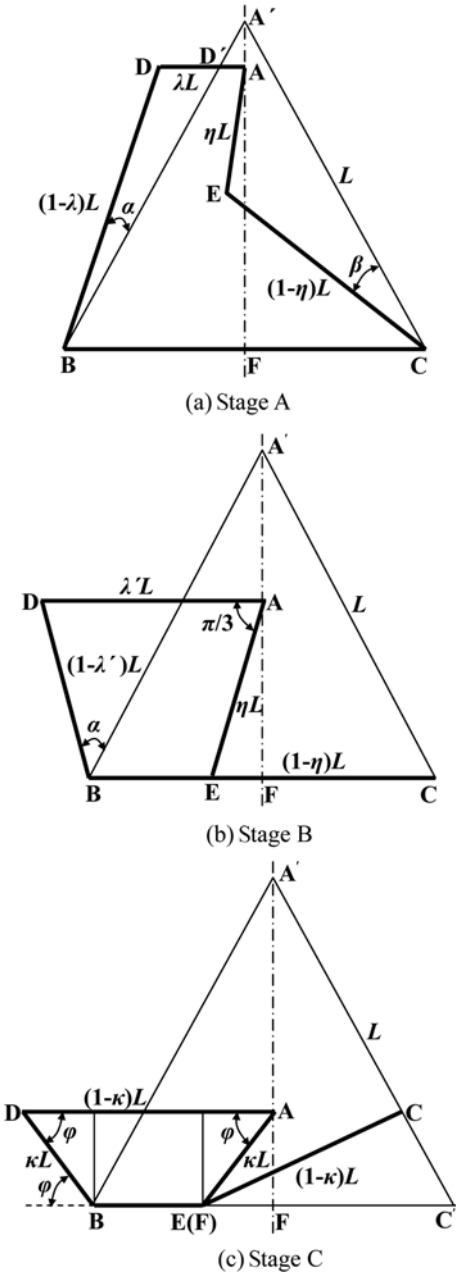

Figure 6. Folding models at (a) stage A, (b) stage B and (c) stage C.

and

$$\frac{P_{mA}}{M_p} = \frac{2\left(\alpha+\beta+\dfrac{\pi}{3}\right)}{\sqrt{3}\lambda L-2(1-\lambda)L\sin\alpha}. \tag{13}$$

Substituting Eq. (9) into Eq. (13), we got

with

$$\tilde{\eta} = \sqrt{3}\eta L + 2(1-\eta)L\sin\left(\frac{\pi}{3}-\beta\right), \tag{15}$$

The length ratio η and the rotation angle α are determined by

$$\frac{\partial P_{mA}}{\partial \eta} = 0, \tag{16}$$

and

$$\frac{\partial P_{mA}}{\partial \alpha} = 0. \tag{17}$$

At the final state of this stage, the parameters are given by

$$\begin{cases} \lambda = 0.38, \alpha = \dfrac{\pi}{9} \\ \eta = 0.31, \beta = \dfrac{\pi}{6} \end{cases}. \tag{18}$$

The crushing displacement is

$$\Delta 1 = 0.234L. \tag{19}$$

The MCF in stage A is predicted by

$$\frac{P_{mA}}{M_p} = \frac{16.41}{L}. \tag{20}$$

3.3. Stage B

In stage B, different plastic deformation mechanism appeared, as shown in Fig. 4. Point A continued to move vertically. Plastic hinge D began to roll to the left horizontally. Length of AD gradually extended while DB was shortened. It is a typical traveling plastic hinge. Plastic hinges B, E and C developed obviously. Side BD rotated outwardly around plastic hinges B while side EC rotated inwardly around plastic hinges C. In this stage, corner A kept its angle as $\pi/3$. At the end of stage B, side EC would contact with the bottom side BC at F. The crushed tube looks like an isosceles trapezoid. Detailed information is listed in Table 1.

The plastic mechanism of stage B is simplified in Fig. 6. Traveling plastic hinge D kept moving horizontally until the angle of corner D turned to $\pi/3$. Rotation angle of corner C, β, increased to $\pi/3$. Accordingly the final angle of corner E was $\pi/3$. At the end of stage B, angle α and β are equal and

$$\alpha = \beta = \frac{\pi}{3}. \tag{21}$$

The total bending energy, W_t, is given by (Lu and Yu, 2003)

$$W_t = \frac{2M_p S}{r}. \tag{22}$$

for the plastic hinge traveling a distance, S, as

$$S = (\lambda' - \lambda)L = (1 - \eta - \lambda)L = 0.31L. \tag{23}$$

To decide the radius of the traveling hinge, r, the arc length is approximate to $L/6$ and the corresponding central angle is $2\pi/3$ from Fig. 6. The radius is given by

$$r = 0.08L. \tag{24}$$

There are also other three plastic hinges developed in stage B. The plastic energy dissipated by them, W_p, is given by

$$W_p = M_p \sum_{i=1}^{3} \varphi_i, \tag{25}$$

with

$$\sum_{i=1}^{3} \varphi_i = \frac{2\pi}{3}, \tag{26}$$

The work done by the MCF, P_{mB}, is equal to the energy dissipated by those two collapse mechanisms, and denoted by

$$P_{mB}\Delta_2 = W_p + W_t = \sum_{i=1}^{3} M_p \varphi_i + \frac{2M_p S}{r}. \tag{27}$$

The crushing displacement in stage B, Δ_2, is given by

$$\Delta_2 = \frac{\sqrt{3}}{2}L - \frac{\sqrt{3}}{2}\eta L - \Delta_1 = 0.342L. \tag{28}$$

The MCF of stage B is predicted by

$$\frac{P_{mA}}{M_p} = \frac{28.78}{L}. \tag{29}$$

3.4. Stages C

In stage C, the force quickly climbed up to a much higher plateau, close or even greater than the initial peak load. Corners of the isosceles trapezoid, A, D, B and E, were completely crushed to zero. Sides FC tipped up until point C contacted with the upper loading cell. Stage C has two new plastic hinges at point F. Deformation before the contact is defined as stage C_1. The subsequent deformation till densification is defined as stage C_2. These two stages have close stresses. Here MCF in stage C, P_{mC}, was predicted by stage C_1. Detailed information is listed in Table 1. Plastic energy dissipated by the four plastic hinges is given by

$$W_p = \sum_{i=1}^{4} M_p \varphi_i , \tag{30}$$

As point C rotated around point E(F) and got same height comparing with point A, the crushing process entered into densification phase. Then the rotated angle is

$$\varphi_i = \frac{\pi}{3} . \tag{31}$$

The two new plastic hinges at point F(E) have a rotation of

$$\varphi_5 = 0.094\pi . \tag{32}$$

The external work done is equal to the product of the mean crushing force and the crushing distance in stage C_1, Δ_{3-1}. Therefore the work balance requires

$$P_{mC}\Delta_{3-1} = \sum_{i=1}^{5} M_p \varphi_i . \tag{33}$$

At the end of stage C_1, the height of the crushed tube, Δ_d, summation of the crush distance in stage C_2, Δ_{3-2}, and the height of the crushed tube at the beginning of the densification, Δ_4, is relating to the radius of the plastic hinge E, which is given by

$$r = \frac{0.31L}{\pi} . \tag{34}$$

The height of the crushed tube at the end of stage C_1 is given by

$$\Delta_d = \Delta_{3-2} + \Delta_4 = 2r = 0.197L. \tag{35}$$

The crushing displacement of stage C_1, Δ_{3-1}, is

$$\Delta_{3-1} = \frac{\sqrt{3}}{2} L - \Delta_1 - \Delta_2 - \Delta_{3-2} - \Delta_4 = 0.093L. \tag{36}$$

The MCF of stage C is predicted by

$$\frac{P_{mC}}{M_p} = \frac{\frac{4}{3}\pi + 0.094\pi \times 2}{0.093L} = \frac{51.46}{L} . \tag{37}$$

3.5. Predictions

Crushing displacements in each stage are listed in Table 2. Compared with tested data, predicted Δ_1 and Δ_d are close, while predicted Δ_2 is greater and predicted Δ_{3-1} is smaller. Predicted mean crushing forces in each stage are consistent with the tested within acceptable errors, as listed in Table 1. Crushing ratio, γ, is defined as ratio of the crushing displacement to the height of the triangle. When γ=0.85, suggested by the experiments, is introduced into Eqs. (20), (29) and (37), the prediction is much more consistent, as shown in Fig. 7, indicating that the simplified plastic model is reasonable and the plastic analysis is efficient for laterally crushed ETTs.

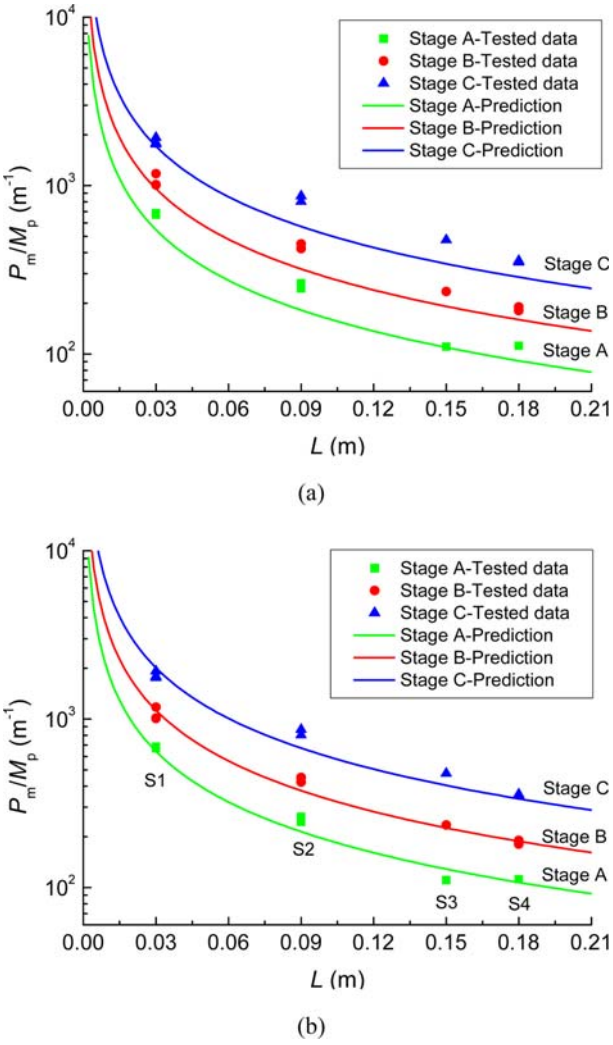

Figure 7. Predicted MCFs for (a) completely crushed tubes and (b) crushed tubes with crushing ratio of 0.85.

4. Numerical Simulations

Commercial finite element method (FEM) software Abaqus/Explicit was applied for crushing simulations. The model was built by shell elements S4R. An imperfection in the right edge was introduced to trigger a non-symmetrical buckling. The imperfection point was located at 0.3L from the top corner, and this point was moved 0.001L to the inward to divide the edge as two lines. The element size is controlled by approximate global size 0.5 mm for S1, and 1 mm for other tubes. Hence, 36000 elements were generated for S1. The number of elements is 13500, 18000, and 27000 for S2, S3 and S4, respectively.

The tube was put on a fixed rigid plane, and another rigid plane was put on the top to compress the tube at a constant velocity. General contact was adopted for the self contact of the triangle tube, and a surface-to-surface

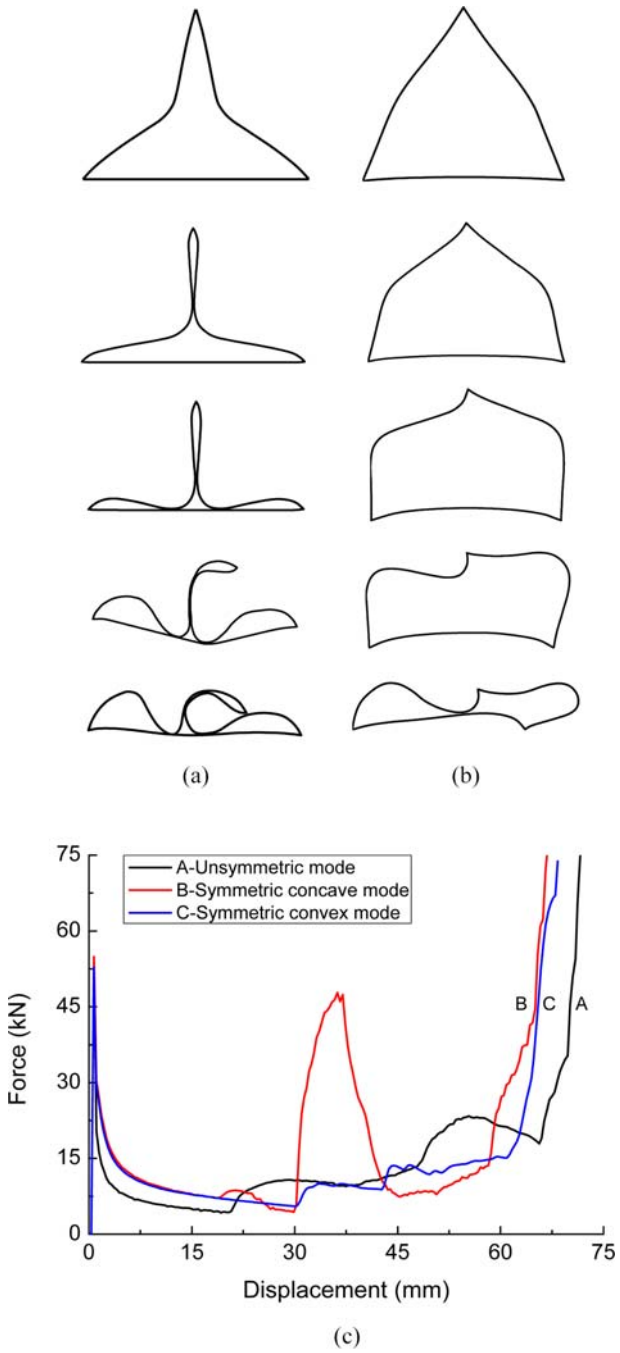

Figure 8. Numerical simulated (a) symmetrical concave deformation mode, (b) symmetrical convex deformation mode and (c) corresponding deformation curves of tube with breadth of 90 mm.

contact was applied between the rigid plane and the tube. Penalty friction formulation was employed for all the contacts with a friction coefficient of 0.15. In experiments, the loading rate, 2.5 mm/min, is too slow for numerical simulations, so that a velocity of 0.125 m/s was adopted in simulation. The quasi-static condition was ensured by keeping the kinetic energy being a small value, less than 0.01% of the internal energy after the buckling.

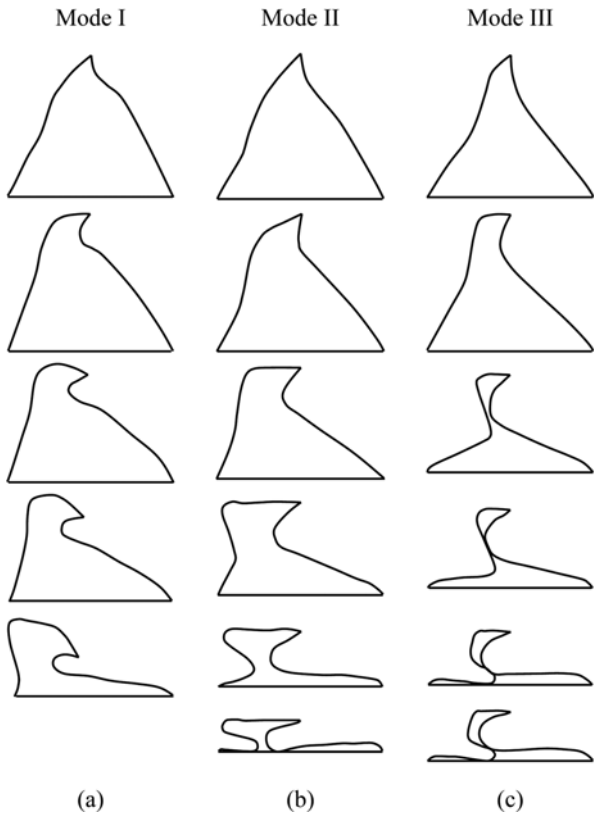

Figure 9. Other non-symmetrical deformation modes suggested by numerical simulation, including: (a) Mode I, (b) Mode II and (c) Mode III .

Correctly predicting the initial peak loads and typical deformation modes in each stage, numerical simulations suggest deformation curves well consistent with the experiments, as shown in Fig. 2, except for the elastic stiffness. All simulations have much greater elastic stiffness, induced by the measurement of the displacement. Instead of being measured by extensometer, the displacement was directly read from the displacement of the load cell of the machine. Including the displacement of the loading system, this measured displacement in elastic stage should be much larger. It must be stressed that the error could be neglected for large plastic deformation.

Without imperfections, symmetrical deformation modes were observed, as shown in Fig. 8. The inclined sides have symmetrical buckles, concave or convex, forming two plastic hinges. In the concave mode, these two hinges move inwardly and finally contact with each other to form a new column, companying with three plastic hinges formed at the three angles. Compression of the column leads a rising load until the column buckles again. So in symmetrical deformation curve there are two comparable peaks. A new plastic hinge forms at the buckle center and lets the tube have another deformation plateau. Convex symmetrical deformation mode displays similar deformation curve as the unsymmetrical deformation mode.

Table 2. Crushing distance in each stage of ETTs

Sample	Tested Δ_1 (mm)	Δ_1 (mm)	Δ_2 (mm)	Δ_2 (mm)	Δ_{3-1} (mm)	Δ_{3-1} (mm)	Δ_{3-2} (mm)	Δ_{3-2} (mm)	$\Delta_d=\Delta_{3-2}+\Delta_4$ (mm)
S1	8.75	7.02	3.58	10.26	3.64	2.79	-	7.59	5.91
S2	23.64	21.06	26.28	30.78	5.15	8.37	9.32	11.15	17.73
S3	34.55	35.10	40.20	51.30	23.85	13.95	7.93	21.79	29.55
S4	43.68	42.12	50.84	61.56	20.62	16.74	20.19	18.29	35.46

Using LS-DYNA, Hong (2013) also found three extra unsymmetrical deformation modes as shown in Fig. 9, not observed in previous experiments. In stage A, they have the same deformation configuration as the tested mode. For mode I, the difference appears in stage B. The traveling plastic hinges do not keep horizontal. Rotation of the line is obvious. For mode II, the difference appears in stage C. The configuration of the plastic mechanism renders the shape of "I". For mode III, there is no traveling plastic hinge in stage B. The inclined sides attract each other and adhere together to shape a plastic hinge. This hinge is the rotation center in stage C.

5. Mean Crushing Forces

5.1. Prediction based on three-stage model

Crushing displacements in each stage are also predicted and compared with the tested data, as listed in Table 2. Crushing distance in stage A, Δ_1, and predicted Δ_{4d} are close to the tested data. Crushing distance in stage B, Δ_2, is greater than the tested data, while predicted Δ_3 in stage C is smaller. Based on the three-stage model, MCF of the tube, P_m, could be predicted by

$$\frac{P_{mC}}{M_p}=\frac{P_{mA}\Delta_1+P_{mB}\Delta_2+P_{mC}\Delta_3}{\Delta_1+\Delta_2+\Delta_3}=\frac{27.6}{L}. \quad (38)$$

Equation (38) can be improved through introducing the crushing ratio, 0.85, into the denominator. Another way is assuming the crushing displacement, Δ, as

$$\Delta=\frac{\sqrt{3}}{2}L-4t, \quad (39)$$

then the MCF is given by

$$\frac{P_m}{M_p}=\frac{\frac{\pi}{3}+\pi+\frac{2\pi}{3}+\pi+\frac{\pi}{3}+\frac{0.61}{0.08}}{\frac{\sqrt{3}}{2}L-4t}=\frac{18.1}{0.866L-0.012}. \quad (40)$$

MCF of the tube is rather close to the MCF in stage B. As shown in Fig. 10, predicted MCFs given by Eqs. (38) and (40) were consistent with the tested data, but the error cannot be ignored, especially for wider ETTs. The model excludes sub-stage C2, which has great influence to MCF of ETTs with longer breadth, such as S2, S3, and S4. To get consistent prediction, crushing ratio, 0.65, must be introduced into the denominator.

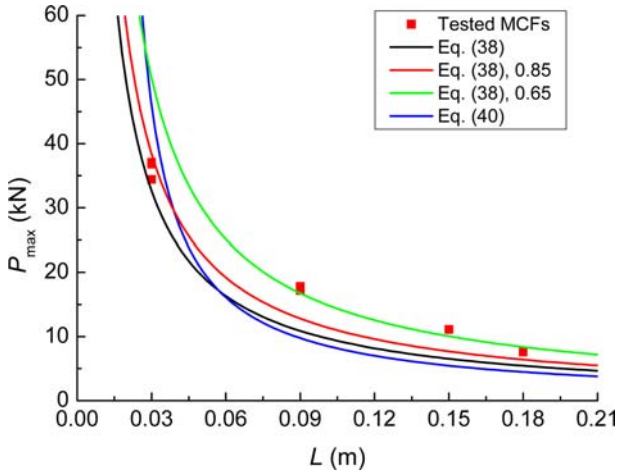

Figure 10. MCF predictions based on three-stage model.

5.2. Prediction based on integral plastic deformation model

To predict the integral mean crushing force of ETTs, crushing distance and energy absorbing mechanism must be clearly revealed and quantitatively described. Suggested by the experiments, the crushing distance, Δ, is defined as

$$\Delta=\frac{\sqrt{3}}{2}\gamma B, \quad (41)$$

where γ=0.85 for thin-walled tubes while γ=0.55 for stout-walled ones.

Five plastic hinges and one traveling plastic hinge were observed in the experiments for most ETTs, although they have different triangular cross sections and deformation modes in stages B and C, as shown in Fig. 11(a). Rotation of the plastic hinge at the apex angle is $\pi/3$. For the two base angles, rotations of the plastic hinges are $2\pi/3$ and $\pi/3$, respectively. At the two buckle centers, each plastic hinge has a rotation of π. Rotation of F is neglected. In crushing, summarized rotation of all these plastic hinges is $10\pi/3$.

Traveling plastic hinge contributes more energy absorption than ordinary plastic hinges. A simplified model is suggested to calculate the radius of the traveling plastic hinge, r, as shown in Fig. 11(b) (Wang *et al*., 2015). According to the

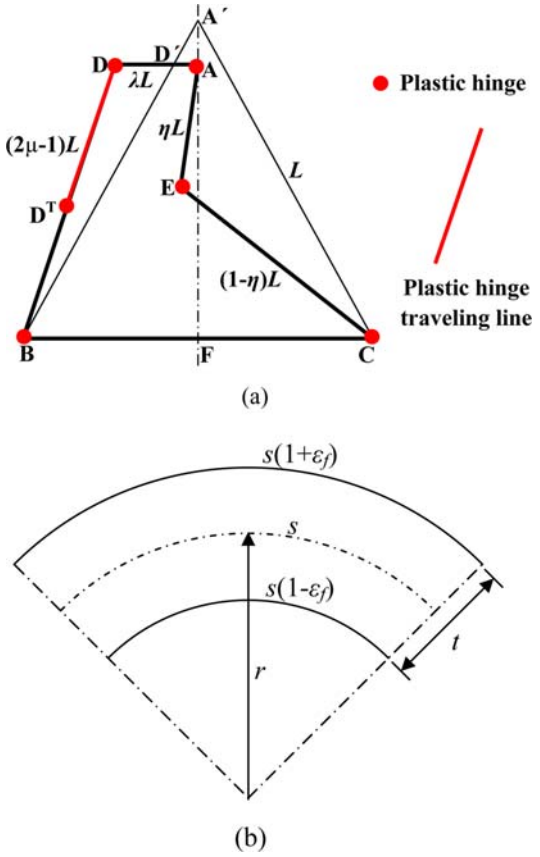

Figure 11. (a) Plastic model and (b) radius calculation of the traveling plastic hinge (Wang *et al*., 2015).

geometry of the traveling plastic hinge, the radius of the traveling plastic hinge is suggested to be

$$\frac{s(1+\varepsilon_f)}{s}=\frac{r+\frac{t}{2}}{r}. \tag{42}$$

where s is the arc length, ε_f is the ultimate strain and ε_f=0.2, suggested by the standard tensile experiment. Radius of the moving plastic hinge is given by

$$r=\frac{t}{2\varepsilon_f}. \tag{43}$$

With t =3 mm and ε_f=0.2, r =7.5 mm. The line length, S, traveled by the plastic hinge is approximately estimated by

$$S=(2\mu-1)B=0.4B. \tag{44}$$

The MCF of ETTs is given by

$$\frac{P_m}{M_p}=\frac{4\pi-2\theta+\frac{2S}{r}}{\frac{\gamma}{2}B\tan\theta}=\frac{100\pi+24\frac{B}{r}}{15\sqrt{3}\gamma B}. \tag{45}$$

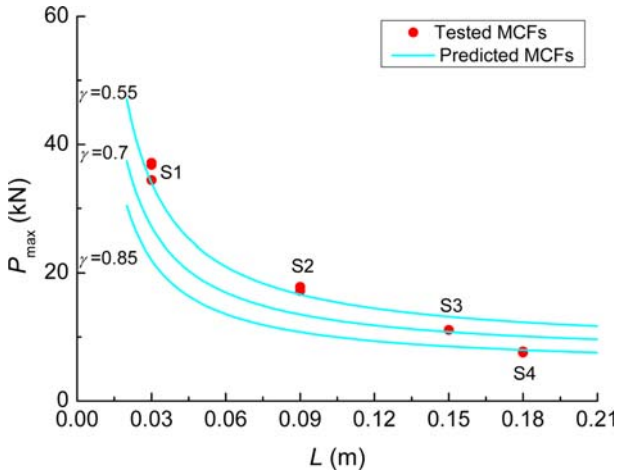

Figure 12. Predicted MCFs of ETTs based on integral plastic deformation model.

As shown in Fig. 12, predicted MCFs of ETTs by Eq. (45) are consistent with tested data with acceptable errors. It is concluded that although the triangles have different geometries, they have similar crushing mechanism. The energy consumption mechanism includes five plastic hinges and one traveling plastic hinge line (DD^T). The energy absorbing property of laterally compressed ETTs is predictable.

6. Conclusions

The paper presented a comprehensive study of lateral compression behaviors of ETTs covering experimental investigations, numerical simulations and theoretical analyses. Reasonable correlations have been shown between theoretical models and experimental observations.

Plastic deformation of laterally compressed ETTs is characterized by three stable plateaus. Stage A is induced by post-buckling plastic deformation of the inclined wall with one end pin-jointed and the other built-in. In stage B, traveling plastic hinge dominates the crushing behavior. In stage C, the mechanism likes a completed crushed isosceles through four plastic hinges at the nodes. Through three-stage deformation, triangular tubes have relatively excellent energy absorptions.

Although ETTs have different geometry and crushing style, they have identical crushing mechanism, including five plastic hinges and one traveling plastic hinge. Plastic models were proposed to predict the MCFs. Compared with the tested data, the theoretical predictions are consistent, indicating that the models correctly capture the nature of the lateral crushing. Moreover, crushing ratio of ETT is important for accurate theoretical prediction for MCF.

Acknowledgments

Supports from the National Natural Science Foundation of China (11172089, 11372095), Fund of State Key Laboratory of Structural Analysis for Industrial Equipment (GZ1002, GZ1306), Funds of State Key Laboratory of Mechanics and Control of Mechanical Structures (MCMS-0212G01, MCMS-0215G01) and Program for New Century Excellent Talents in University are gratefully acknowledged.

References

Abdewi, E. F., Sulaiman, S., Hamouda, A. M. S., and Mahdi, E. (2008). "Quasi-static axial and lateral crushing of radial corrugated composite tubes." *Thin Wall. Struct.*, 26, pp. 320-332.

Fan, Z., Lu, G., Yu, T. X., and Liu, K. (2013). "Axial crushing of triangular tubes." *Int. J. Appl. Mech.,* 5, pp. 1350008-1-1350008-21.

Ferri, E., Antinucci, E., He, M. Y., Hutchinson, J. W., Zok, F. W., and Evans, A. G. (2007). "Dynamic buckling of impulsively loaded prismatic cores." *J. Mech. Mater. Struct*., 1(8), pp. 1345-1365.

Gupta, N. K., Sekhon, G. S., and Gupta, P. K. (2001). "A study of lateral collapse of square and rectangular metallic tubes." *Thin-Walled Structures,* 39, pp. 745-772.

Hong, W. (2013). *Axial collapse of thin-walled, single- and multi-cell tubes with triangular cross section*. Dissertation, PLA University of Science and Technology, Nanjing.

Hong, W., Fan, H. L., Xia, Z. C., Jin, F. N., Zhou, Q., and Fang, D. N. (2014). "Axial crushing behaviors of multi-cell tubes with triangular lattices." *Int. J. Impact Eng*., 63, pp. 106-117.

Hong, W., Jin, F. N., Zhou, J. N., Xia, Z. C., Xu, Y., Yang, L., Zheng, Q., and Fan, H. L. (2013). "Quasi-static axial compression of triangular steel tubes." *Thin Wall. Struct.*, 62, pp. 10-17.

Hou, S. J., Han, X., Sun, G. Y., Long, S. H., Li, W., and Yang, X. J. (2011). "Multiobjective optimization for tapered circular tubes." *Thin Wall. Struct.*, 49, pp. 855-863.

Hou, S. J., Li, Q., Long, S. Y., Yang, X. J., and Li, W. (2008). "Multiobjective optimization of multi-cell sections for the crashworthiness design." *Int. J. Impact Eng*., 35, pp. 1355-1367.

Jones, N. (1989). "Recent studies on the dynamic plastic behavior of structures." *Appl. Mech. Rev.,* 42(4), pp. 95-115.

Lee, S., Barthelat, F., Hutchinson, J. W., and Espinosa, H.D. (2008). "Dynamic failure of metallic pyramidal truss core materials-experiments and modeling." *Int. J. Plasticity,* 22, pp. 2118-2145.

Lu, G. X. and Yu, T. X. (2003). *Energy absorption of structures and materials*. Cambridge, Wood-head, UK.

Mahdi, E. and Hamouda, A. M. S. (2012). *Energy absorption capability of composite hexagonal ring systems*. Mater. Des., 34, pp. 201-210.

McShane, G. J., Pingle, S. M., Deshpande, V. S., and Fleck, N. A. (2012). "Dynamic buckling of an inclined strut." *Int. J. Solids Struct*., 49, pp. 2830-2838.

Radford, D. D., Deshpande, V. S., and Fleck, N. A. (2009). "The use of metal foam projectiles to simulate shock loading on a structure." *Int. J. Impact Eng*., 31, pp. 1152-1171.

Rejab, M. R. M. and Cantwell, W. J. (2013). "The mechanical behaviour of corrugated-core sandwich panels." *Compos. Part B Eng*., 47, pp. 267-277.

Tran, T. N., Hou, S. J., Han, X., Tan, W., and Nguyen, N.T. (2014). "Theoretical prediction and crashworthiness optimization of multi-cell triangular tubes." *Thin Wall. Struct*., 82, pp. 183-195.

Wang, P., Zheng, Q., Fan, H. L., Sun, F. F., Jin, F. N., and Qu, Z. X. (2015). "Quasi-static crushing behaviors and plastic analysis of thin-walled triangular tubes." *J. Constr. Steel Res*., 106, pp. 35-43.

Zhang, X. and Zhang, H. (2012). "Energy absorption limit of plates in thin-walled structures under compression." *Int. J. Impact Eng*., 24, pp. 121-131.